

# Metal Anode Performance in Low-Temperature Electrolytes for Aluminum Production

T.R. BECK, C.M. MacRAE, and N.C. WILSON

An investigation has been undertaken into the performance of metal alloy anodes used to produce aluminum *via* an electrochemical method. Alumina was electrolyzed in NaF/AlF<sub>3</sub> and KF/AlF<sub>3</sub> electrolytes and mixtures thereof with copper-nickel-iron (Cu:Ni:Fe) alloy anodes and titanium diboride (TiB<sub>2</sub>) cathodes. The operating temperatures of the electrochemical cells ranged from 973 K to 1123 K (700 °C to 850 °C), with an anode current density of 5000 A/m<sup>2</sup>. Cells ranged in current capacity from 10 to 300 amperes, with oxygen gas formed at the anode and molten aluminum collected from the cathode. Posttest anodes were sectioned, and elemental maps were performed to characterize the distribution of the chemical phases, including the metal electrodes, bath phases, and aluminum metal production, which were used to determine the reaction mechanisms of the cell. The metal alloy slowly corroded and formed an adherent, electronically conducting nickel ferrite plus copper scale during the operation of the cell. The proposed mechanisms of the anode performance are described herein.

DOI: 10.1007/s11663-011-9511-8

© The Minerals, Metals & Materials Society and ASM International 2011

## I. INTRODUCTION

TO reduce energy consumption by lowering the operating temperature of aluminum production cells, a series of tests were carried out in the late 1970s using composite anodes containing stoichiometric alumina in carbon anodes,<sup>[1–3]</sup> which allowed for a variety of electrolytes and operating temperatures as low as 973 K (700 °C). In these test cells, alumina was fed directly to the site of consumption on the active anode surface, which meant the electrolyte did not require high alumina solubility. However, this technology did not gain acceptance in the industry because the anodes required larger baking furnaces and had a higher electrical resistance. Continued development resulted in an inert cermet anode consisting of nickel ferrite and copper<sup>[4]</sup> being developed by Alcoa (Pittsburgh, PA) in the early 1980s to replace the consumable carbon anodes in the Hall–Heroult process.

A concept that combined both ideas from the previous work was patented<sup>[5]</sup> in 1989. This process involves the inert anodes being used in a low-temperature fluoride electrolyte containing a slurry of alumina, which brings alumina particles in direct contact with the anode surface from the electrolyte side. The primary reaction on the anode surface is the formation of oxygen gas and aluminum ions in the electrolyte. One key advantage of this concept is that a battery of vertical cermet anodes and titanium diboride cathodes would result in a compact cell in comparison with the Hall–

Heroult cell. The cell construction is similar to that of modern chlor-alkali cells and aqueous metal refining cells. In subsequent work,<sup>[6–8]</sup> it was found that anodes of the Cu:Ni:Fe alloy could be used instead of cermet, and an extensive test program followed from 1998 to 2003 employing a range of Cu-Ni-Fe anode compositions as well as NaF/AlF<sub>3</sub> and KF/AlF<sub>3</sub> electrolyte compositions.<sup>[9–11]</sup> Current efficiencies of up to 95 pct and aluminum purities of up to 99.5 pct were achieved in 200-ampere cells. The high metal purity<sup>[9]</sup> shows that little corrosion of the alloy anode occurred. Elemental maps of cross sections of anode/electrolyte surfaces were undertaken, the results of which are presented here.

## II. EXPERIMENTAL

### A. Experimental Cell Tests

An extensive test program of test cells was made with Cu:Ni:Fe alloy anodes and titanium diboride cathodes in a laboratory in Seattle, WA and in laboratories at aluminum plants at Goldendale, WA and The Dalles, OR.<sup>[9]</sup> A range of anode alloy compositions and structures including sintered, two-phase as cast, and homogenized were employed. Electrolyte compositions were eutectic NaF:AlF<sub>3</sub> and KF:AlF<sub>3</sub> as well as mixtures thereof. The cathode material employed in the cells was titanium diboride, and operating temperatures ranged from 973 K to 1123 K (700 °C to 850 °C) with cell sizes varying from 10 ampere to 300 amperes and test durations varying from 6 to 300 hours.

### B. Electron Probe Mapping

Selected posttest anodes with some electrolyte still in intimate contact were examined by electron probe

T.R. BECK, President, is with ETCI LLC, Seattle, WA 98125. C.M. MacRAE, Director Microbeam Laboratory, and N.C. WILSON, Electron Microscopist/Microanalyst, are with CSIRO Process Science and Engineering/CSIRO Light Metals Flagship, Clayton, Victoria 3168, Australia. Contact e-mail: colin.macrae@csiro.au

Manuscript submitted October 5, 2010.

Article published online April 13, 2011.

microanalysis and were prepared into polished cross sections. At the conclusion of a test cell run, the voltage was switched off and the anode was removed with a film of some adhering electrolyte. Previously, an experiment was reported in which a whole frozen cell was examined.<sup>[11]</sup> At the conclusion of that test, the heater was turned off and the cell switched to a constant voltage mode to freeze the bath and retrain the approximate distribution of chemical phases in the cell. These cells were then back filled with epoxy to encapsulate the reactive phases. The whole cell samples had the advantage that the chemistry across the entire cell could be examined and an understanding of the chemical profiles could be imaged.

Metal alloy anode samples were sectioned across the interfacial region with a low-speed diamond saw using an oil lubricant. The sections were then ground back on diamond impregnated grinding disks, with a final diamond size of 6  $\mu\text{m}$ . Then ground sections were polished on pads with diamonds in suspension, with the final size being 1  $\mu\text{m}$ . The advantage of this technique over preparation with sandpaper was that the surface was optically flat over large distances. Typically, the dissimilar hardness materials like titanium diboride and electrolyte usually grind at different rates resulting in significant topography, which is undesirable for electron microprobe mapping. Prior to analysis in the electron microprobe, the samples were coated with 15 to 20 nm of carbon.

Elemental maps were acquired on a JEOL 8900R Superprobe (JEOL, Tokyo) electron microprobe analyzer equipped with one energy dispersive and five wavelength dispersive spectrometers (WDS). Large area maps were obtained using a grid of analysis points for the elements Fe, O, Ti, Mg, Al, Cu, Na, K, Si, Ca, P, and F, which were all measured by WDS. Two passes were performed, and the light elements, Na, F, O, Al, and P were measured on the first pass to minimize migration effects from the electron beam. Standards used to calibrate the spectrometers were hematite (**Fe<sub>2</sub>O<sub>3</sub>**), rutile (**TiO<sub>2</sub>**), Mg-Al spinel (**MgAl<sub>2</sub>O<sub>4</sub>**), copper and nickel metal, sodium chloride (**NaCl**), adularia (**KAlSi<sub>3</sub>O<sub>8</sub>**), wollastonite (**CaSiO<sub>3</sub>**), apatite (**Ca<sub>5</sub>(PO<sub>4</sub>)<sub>3</sub>F**), and cryolite (**Na<sub>3</sub>AlF<sub>6</sub>**). Elements marked in bold were collected from the standards. Mosaic maps comprising three or four individual maps were collected across each anode sample, which were then combined, giving a typical coverage of  $\sim 6 \times 9$  mm. Maps were collected with an accelerating voltage of 15 kV, a regulated beam current of 100 nA, a step size of 2  $\mu\text{m}$  (in both  $x$  and  $y$  directions), and a dwell time of 15 ms per step. Each  $\sim 6.0 \times 9.0$  mm map took a minimum of 12 hours to acquire.

#### 1. Bence-Albee matrix correction procedure

The mapping procedure used in this study involved collecting the X-rays on the element peaks only and scaling these for counting time and beam current and then dividing them by the count rates collected on standards of known composition. These scaled values are referred to as “k-ratio” levels. When collecting X-rays in this fashion, one needs to consider the effects

of the matrix on the X-ray signal. By far, the largest effect on observed X-ray intensity is caused by absorption. A single pass correction for absorption was applied to the k-ratio's measured at each pixel based on the Bence-Albee correction procedure.<sup>[12]</sup> In interpretation of results, the accuracy for Cu, Ni, and Fe is about 2 pct, but the accuracy for Ti, Na, P, K, Al, F, and O is only 20 pct or higher.

#### 2. Manual phase selection

Electron microprobe maps were manipulated using the CSIRO Chimage<sup>[13]</sup> software package. This software enables complete processing and interpretation of the data set offline. Elemental data can be displayed as elemental scatter plots, and clusters corresponding to individual chemical phases can be identified from a built-in mineral database. Data points comprising each cluster were manually selected, and the chemical phase represented by the cluster was defined and saved before displaying the complete set of data as a phase-patched map.

For a complex assembly of compounds, it can be difficult to assign all points manually to chemically distinct phases. Several detrimental processes can occur that lead to increased scatter in elemental plots; they are the beam straddling two or more phases, and the beam stepping across the edge of a particle or surface into the mounting epoxy. Voids or holes in the sample also lead to changes in X-ray-to-detector path length, which can lead to enhanced or reduced signals from rims, which also scatters the results. However, assignment of phases is still possible and one key advantage of the mapping data is that, where scatter occurs, it is possible to confirm its origin by relocating the points on the sample.

#### 3. Automatic phase selection

Phases containing minor elements and those with many elements require several elemental scatter plots to be examined simultaneously, which increases the difficulty of the manual phase assignment. One approach to this problem is implementing auto cluster selection algorithms.<sup>[14]</sup> Such algorithms allow for the selection of clusters in multidimensional space, which minimizes operator bias and aids in the interpretation and characterization of the various chemical phases. One can select the required number of clusters and allow the computer to do the clustering. With this approach, all points in the map are associated with one phase, no points are missed, and no multiple assignments of points occur.

### III. RESULTS AND DISCUSSION

Results are presented for a typical run with a 40:30:30 weight ratio Cu:Ni:Fe anode in 55:45 mol ratio KF:AlF<sub>3</sub> eutectic electrolyte (Figure 1). The cell operating temperature was 973 K (700 °C), and the eutectic melting point was approximately 833 K (560 °C). Vertical sheet electrodes were used in a 300-ampere cell for a 100-hour run.

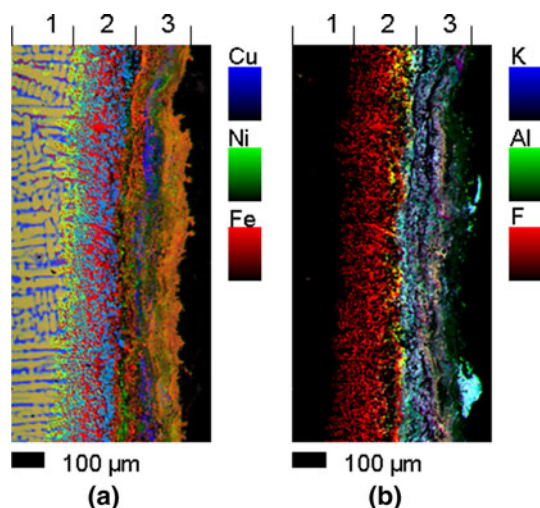


Fig. 1—Three color elemental maps of an anode cross section after electrolysis. (a) Plot of Cu, Ni, and Fe, and (b) shows K, Al, and F from the same region. Base alloy, corrosion, and scale regions are labeled 1, 2, and 3, respectively. Several reaction layers are clearly visible, illustrating the complexity of the anode-bath electrolysis.

Element maps are plotted as three-color maps for Cu, Ni, and Fe and for K, Al, and F and are shown in Figures 1(a) and (b). The three-color maps reflect the concentration of the individual elements, and when a combination of elements occurs at a pixel, the colors are mixed. For example, when elements labeled as green and red both present, the resulting color is yellow, whereas red and green with some blue will lead to a brown color. Compositions in three regions are examined and labeled as the base alloy (1), the porous iron and nickel corrosion region (2), and the scale (3) in Figure 1(a). The base alloy anode consisted of two main phases—an iron-nickel-copper phase (yellow–brown) and a high copper, low iron-nickel phase (blue). Iron is corroded preferentially from the iron-rich phase in the alloy, initially leaving an enriched nickel phase behind. The copper-rich phase (blue) is not corroded in this zone. The corroded iron forms a fluoride, as shown by coexisting F in Figure 1(b), which is more clearly shown in the phase map (Figure 2) where the iron fluoride phase is indicated in red. The iron fluoride regions (Figure 2 [red]) seem to be corrosion pathways or tunnels. This tunnel corrosion mechanism of the iron-rich phase was observed in other similar tests with two-phase Cu-Ni-Fe alloys. The orange-red layer (Figure 1a, region 3) in the inner part of the scale and the orange layer in the outer part of the scale are enriched in nickel and somewhat depleted in iron compared with the red phase, an iron fluoride, in the porous metal.

The compositions of the three metals in the alloy, porous metal, and scale are given in Table I. Calibration was based on the average 40:30:30 composition in the alloy metal. A modal analysis of the phase patched image (Figure 2) shows that the base alloy metal has an area percentage of 15 pct copper-rich phase and 85 pct iron-rich phase, resulting in the distribution of Cu, Ni, and Fe shown in the two phases. It was noted that the copper-rich phase remains nearly unchanged from the

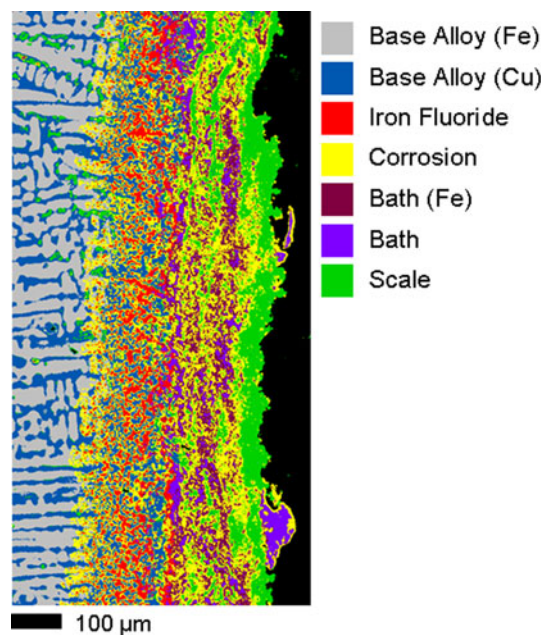


Fig. 2—Chemical phase patched image of the mapped region. Phases have been identified based on their chemical composition.

**Table I. Compositions of the Three Metals in the Alloy, Porous Metal, and Scale Taken from Cluster Centroids in Elemental Scatter Plots**

	Alloy Average	Alloy Phases		Porous Metal			Scale	
		Yellow	Blue	Green	Blue	Red	Blue	Orange
Cu	40	24	75	20	69	7	80	10
Ni	30	37	14	52	23	2	13	29
Fe	30	39	11	28	8	91	7	61

base alloy through the porous metal layer into the scale. The Ni-rich zone at the boundary of the base layer in the porous metal is depleted in iron and thus is enriched in nickel. The electrolyte layers (Figure 2) have been grouped into two compositions, and predominately, the higher iron-containing electrolyte phase is farther out in the scale-corrosion region, indicating an effective transportation of the iron fluoride away from the tunnels.

Corrosion tunnels did not form in a thermally homogenized 40:30:30 Cu:Ni:Fe alloy for the same electrolysis conditions. The iron-nickel-copper phase (brown) in Figure 1(a) may have defects that enabled the nucleation of tunnels resulting in corrosion. An alternative explanation is that a threshold composition exists between 40:30:30 Cu:Ni:Fe and the composition in the Figure 1(a) iron-nickel-copper phase, 24:37:39 (Table I) for tunnel corrosion to occur.

Figure 3, shows an elemental scatter plot of nickel vs oxygen and a O, Ni, Fe three-color map. The nickel-iron oxide phase has been highlighted in the scatter plot and these same pixels are colored in the three-color map, with the remaining pixels in grey. This illustrates that the outer scale layer is mainly an oxide in nature rather



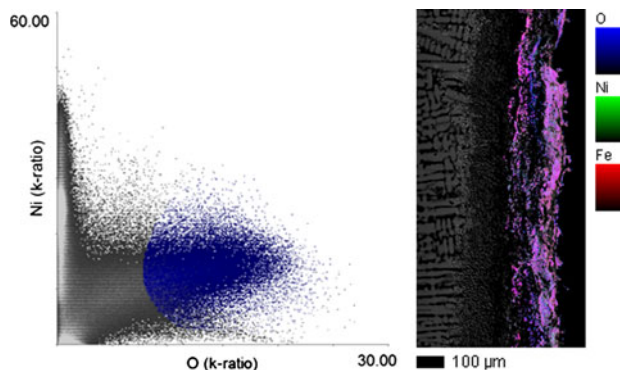
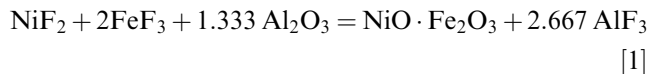


Fig. 3—Elemental scatter plot of Ni vs O with the nickel-iron oxide pixels selected in blue. The selected pixels projected on the O, Ni, and Fe map are highlighted. This shows that the scale layer has an oxide nature.

than a fluoride. The highlighted cluster in Figure 3 has a composition of Cu 7.2 wt pct, Fe 41.3 wt pct, Ni 23.9 wt pct, and O 26.5 wt pct, giving a formula of  $\text{Ni}(\text{Cu}, \text{Fe})_2\text{O}_4$ , which is confirmed by X-ray diffraction on scrapings of the scale that showed the presence of a nickel ferrite ( $\text{NiFe}_2\text{O}_4$ ). The free energy of nickel ferrite formation at 973 K (700 °C) from  $\text{NiF}_2$ ,  $\text{FeF}_3$ , and  $\text{Al}_2\text{O}_3$  from the bath is expressed as follows:



and is  $-27.928 \text{ kcal}$ ,<sup>[15]</sup> making nickel ferrite  $\text{NiFe}_2\text{O}_4$  a thermodynamically likely product. The scale seems to be a cermet of nickel ferrite with metallic copper particles on a ductile metal substrate. The ragged outer surface in Figure 1a suggests that oxygen bubble evolution may pluck out bits of scale, which leads to a wear mechanism. This mechanism plus the dissolution of the metal ions may limit the thickness of the scale.

A calculated electromotive series for the compounds of interest in the interpretation of reactions occurring on the surface of a Cu:Ni:Fe anode is shown in Table II. The free energies of formation are from HSC Chemistry<sup>[15]</sup> and the JANAF Tables<sup>[16]</sup> for a temperature of 1000 K (727 °C). Molten aluminum is the reference electrode, which is preferred because it is the cathode of a cell and it has a small overpotential during electrolysis.

The observed sequence of corrosion of the metals in the anode is consistent with the electromotive series in Table II. Iron corrodes first within the base alloy surface, then nickel, and then copper. A summary of the proposed reactions in and on the anode surface that are consistent with the electromotive series is presented in Figure 4. The standard potentials in Figure 4 are based on  $E_{\text{Al}} = 0$  as well as unit activities of reactants and products. The actual potentials would be slightly different but not known exactly because the activities of reactants and products may differ somewhat from unity.

Corrosion tunnels are filled with solid  $\text{FeF}_2$  (melting point  $>1273 \text{ K}$  [ $1000 \text{ °C}$ ]) that bore into the iron-rich phase of the alloy anode. Figure 5 shows an elemental scatter plot of iron vs fluorine as well as a Cu, Ni, and Fe

**Table II. Electromotive Series for Aluminum Electrolysis at 1000 K (727 °C) Based on Free Energies of Formation of Compounds in JANAF Tables<sup>[16]</sup> F2 and O2 Are Ideal Gases at One Atmosphere. All Other Compounds Are in Pure Standard Crystalline State Except Al, Which Is in Liquid State\***

Compound	Electrons (n)	$\Delta G_f^0$ (kcal/mol)	$E^0$ (V)	$E^0$ (V, Al = 0)
Basis $E^0$				
$\text{AlF}_3$	3	-298.767	4.319	4.319
$\text{Al}_2\text{O}_3$	6	-325.301	2.351	2.351
Derived $E^0$ (V, Al = 0)				
$\text{CuF}$	1	-30.881	1.339	2.980
$\text{CuF}_2$	2	-93.140	2.020	2.300
$\text{CuO}$	2	-15.923	0.345	2.006
$\text{Cu}_2\text{O}$	2	-23.094	0.501	1.850
$\text{NiF}_2^\dagger$	2	-120.047	2.603	1.716
$\text{NiO}^\dagger$	2	-35.657	0.733	1.578
$\text{Fe}_2\text{O}_3$	6	-134.363	0.971	1.380
$\text{FeF}_2$	2	-135.796	2.944	1.375
$\text{FeO}$	2	-49.495	1.073	1.278
$\text{SiO}_2$	4	-174.561	1.893	0.458
Al				0.000
KF	1	-110.843	4.806	-0.487
NaF	1	-112.636	4.885	-0.566
$\text{CaF}_2$	2	-248.851	5.396	-1.077

$E^0$  (Al = 0) =  $4.319 - E^0$  for fluoride compounds.

$E^0$  (Al = 0) =  $2.351 - E^0$  for oxide compounds.

Potentials at other than unit activity of products and reactants.

$E = E^0 - [2.303 \text{ RT/nF}] \log (a_p/a_r)$ .

@  $T = 1000 \text{ K}$  (727 °C).

$E = E^0 - [0.198/\text{n}] \log (a_p/a_r)$ .

\* $E^0 = -\Delta G_f^0/23.060 \text{ n}$ .

<sup>†</sup>From HSC Chemistry.<sup>[15]</sup>

three-color map. The iron fluoride phase has been highlighted in the scatter plot and these same pixels are colored in the three-color map, with the remaining pixels in grey. This figure shows that the main phase in the corrosion region is an iron fluoride compound.

The proposed mechanism in the tunnels is that fluoride ions are brought in by electrolytic migration through solid  $\text{FeF}_2$  to the ends of the tunnels. The standard potential at the ends of the tunnels to form  $\text{FeF}_2$  is 1.375 V according to Table II. At the porous metal-scale interface,  $\text{Fe}^{2+}$  in  $\text{FeF}_2$  is oxidized to  $\text{Fe}^{3+}$  in  $\text{FeF}_3$  at 1.745 V, and nickel is oxidized to  $\text{Ni}^{2+}$  in  $\text{NiF}_2$  at 1.716 V. The outer surface of the scale is at a potential of 2.351 V for the oxidation of  $\text{Al}_2\text{O}_3$  to  $\text{O}_2$  and  $\text{Al}^{3+}$ , plus an overpotential  $\eta$  of perhaps a few tenths of a volt. Copper particles, which break out of the porous metal layer, are oxidized to  $\text{Cu}^{2+}$  at a potential of 2.300 V near the outer part of the scale. The scale is electronically conducting but apparently porous enough for fluoride ions and alumina or for aluminum oxy-fluoride to diffuse in.

The nickel ferrite and copper in the scale are electronic conductors, allowing the alumina to discharge at the scale-electrolyte interface to form oxygen as shown in Figure 4. This is the dominant reaction as the corrosion reactions of Fe, Ni, and Cu have accounted for as little as 0.5 pct of the impurities in the aluminum produced during 300-hour runs.<sup>[9]</sup> If oxygen were

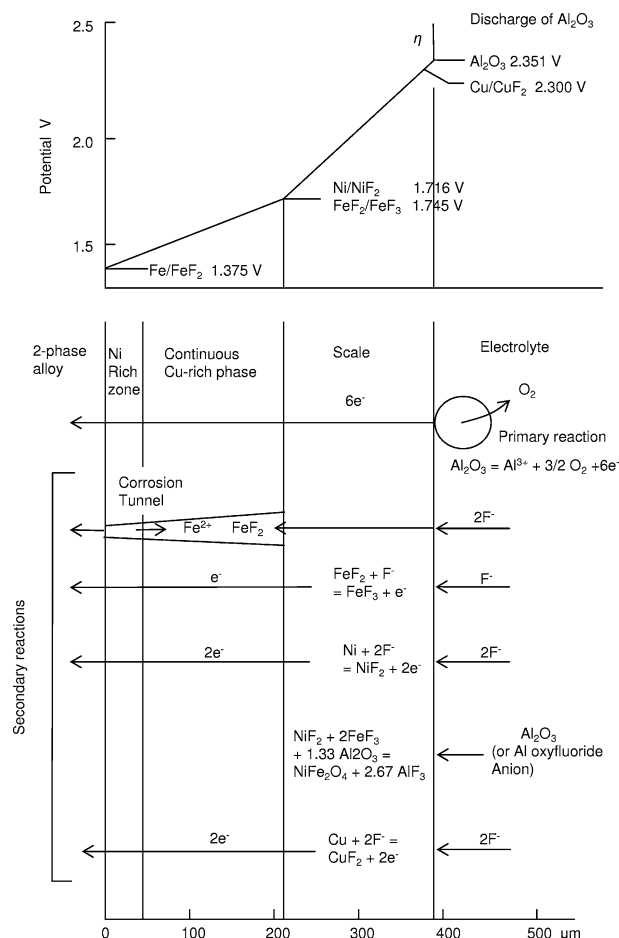


Fig. 4—Summary of proposed reactions in and on an anode surface consistent with elemental maps in Fig. 1 and electromotive series in Table II.

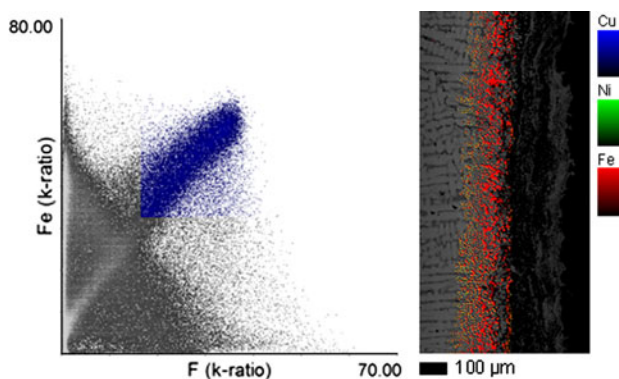


Fig. 5—Elemental scatter plot of Fe vs F with the iron fluoride pixels selected in blue. The selected pixels projected on the Cu, Ni, and Fe map are highlighted. This shows that the corrosion region is rich in iron fluoride.

formed within the scale, then the scale would be “blasted off.” Stoichiometric  $\text{NiFe}_2\text{O}_4$  may not be a good electronic conductor at 973 K (700 °C), but the nonstoichiometric forms deficient in Fe are conductive.<sup>[4]</sup> The conduction of 5000 A/m<sup>2</sup> through a scale of

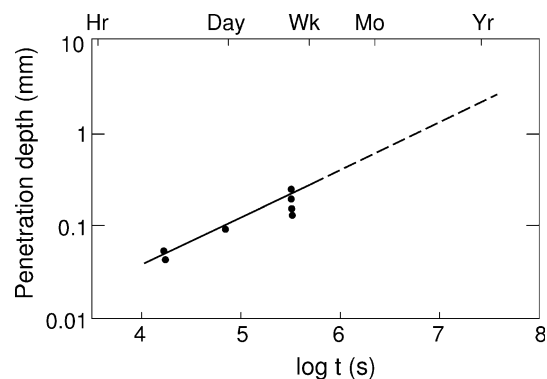


Fig. 6—Corrosion penetration depth into an alloy as a function of time.

160-μm thick, with a conductivity between 1000 and 10,000  $\Omega^{-1} \text{ m}^{-1}$  and no porosity, would give a potential drop of less than 0.0008 V, which is desirable for a high-efficiency anode.

The rate-limiting step for growth of the scale on the surface of the anode is not known for certain, but the growth of the tunnels in Figure 1 seems to be a likely candidate. The initial penetration depth of the corrosion tunnels into the anode alloy, for runs at 973 K (700 °C), follows the subsequent empirical half power law with time  $t$ , as shown in Figure 6:

$$l = (kt)^{1/2} \quad [2]$$

This relation is consistent with one-dimensional, solid-state diffusion of a species in a growing tunnel. Crank<sup>[17]</sup> gives the following relation:

$$x/(4Dt)^{1/2} = \text{constant} \quad [3]$$

for one-dimensional diffusion in a semiinfinite solid where  $x$  is distance (cm),  $D$  is the diffusion coefficient ( $\text{cm}^2/\text{s}$ ), and  $t$  is time (s). An examination of values of the error function in Crank indicate that the constant has a value near unity. Fitting Eq. [3] to Figure 6 results in a value of  $D$  equal to  $3 \times 10^{-10} \text{ cm}^2/\text{s}$ . The actual value is larger than this because the fractional cross section for the diffusion of  $\text{Fe}^{2+}$  or  $\text{F}^-$  in  $\text{FeF}_2$  in the tunnels is less than unity. For example, the value of  $D$  may be as large as  $1 \times 10^{-9} \text{ cm}^2/\text{s}$ . It is expected that, given enough time, the rate of penetration would slow to the corrosion rate of the nickel component at the metal-scale interface and the tunnel length would become constant; however, tests were not long enough to verify this expectation.

Values of  $k$  for four tests in which conditions were the same except for temperature are linear on semilogarithmic coordinates in Figure 7. The extrapolated value of  $k$  to 1223 K (950 °C) is about  $10^4$  greater compared with 973 K (700 °C), illustrating the advantage of low-temperature electrolysis for metal anodes. One test with a thermally homogenized alloy at 973 K (700 °C) resulted in a value of  $k$  reduced by a factor of ten. No corrosion tunnels were found, only a gradient in concentration of iron within the surface of the alloy.

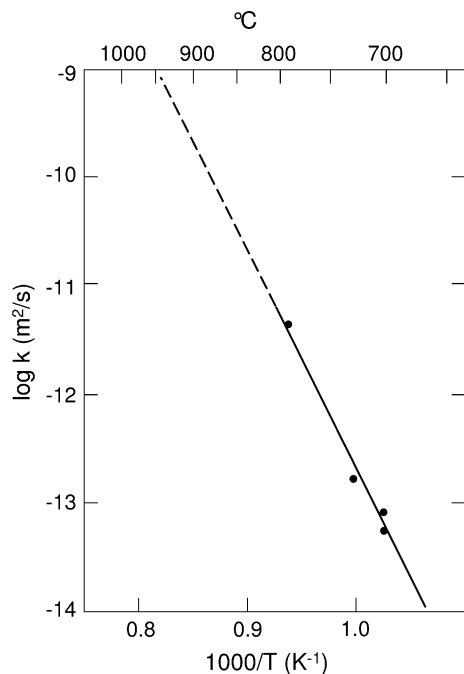


Fig. 7—Corrosion rate constant as a function of temperature.

The rate-limiting step apparently changed to solid-state diffusion of iron in the homogeneous alloy to the interface with electrolyte in the scale rather than through solid  $\text{FeF}_2$  in tunnels. The value of this diffusion coefficient calculated by Eq. [3] was about  $4 \times 10^{-12} \text{ cm}^2/\text{s}$ . This value is consistent with the order of magnitude values of  $D$  for diffusion of Fe in each of Cu, Ni, and Fe at a temperature of 973 K (700 °C) calculated from Smithells,<sup>[18]</sup> who found the self-diffusion of  $\alpha$ -Fe to be  $2 \times 10^{-13} \text{ cm}^2/\text{s}$ ; Fe in Cu to be  $4 \times 10^{-12} \text{ cm}^2/\text{s}$ ; and Fe in Ni to be  $6 \times 10^{-15} \text{ cm}^2/\text{s}$ .

A practical result determined during the study reported here is that molten aluminum crept above the electrolyte level on cylindrical titanium diboride ( $\text{TiB}_2$ ) cathodes in the 10-ampere cells. This aluminum was exposed to oxygen and air and was reoxidized, decreasing the current efficiency. A tight-fitting alumina sleeve placed over the top of the cathode above the electrolyte prevented this reoxidation and measured current efficiencies were above 90 pct. The low current efficiencies of 20 to 80 pct reported in earlier work<sup>[7]</sup> were attributed to aluminum falling off the cathodes and resting on the bottom anode. It is now realized that the interfacial tensions among aluminum,  $\text{TiB}_2$ , and electrolyte held the ball of aluminum on the bottom of the cathode during the 7-hour tests and that aluminum crept up the cathodes to the gas above caused the low current efficiencies.

Frazer and Thonstad<sup>[19]</sup> recently showed that alumina solubility is 2 pct higher in KF- $\text{AlF}_3$  eutectic than in NaF- $\text{AlF}_3$  eutectic at about 1023 K (750 °C). They suggest that an alumina slurry may not be needed in KF- $\text{AlF}_3$  eutectic to avoid the anode effect. The following three modes of mass transfer of alumina to the metal alloy anode are available: by well-known convection of electrolyte past the anode caused by rising oxygen bubbles, by detachment of oxygen bubbles and

inflow of electrolyte,<sup>[20]</sup> and by impinging small alumina particles.<sup>[7]</sup> The latter may indeed not be necessary for a sufficient mass-transfer rate in KF- $\text{AlF}_3$  eutectic electrolyte. Nevertheless, the supersaturation of electrolyte by alumina particles would be necessary to prevent the alumina sleeves from dissolving, if used.

#### IV. CONCLUSIONS

In this study, laboratory experiments with metal alloy anodes have been used to produce aluminum. Alumina was electrolyzed in NaF/ $\text{AlF}_3$  and KF/ $\text{AlF}_3$  electrolytes and mixtures thereof with copper-nickel-iron (Cu:Ni:Fe) alloy anodes and titanium diboride cathodes. Operating temperatures of the cells ranged from 973 K to 1123 K (700 °C to 850 °C), with anode current densities of up to 5000 A/m<sup>2</sup>, and cells ranged in size from 10 to 300 amperes. Oxygen gas formed at the anode and molten aluminum and was collected from the cathode. An electron microprobe of the anode sections revealed that the base alloy slowly corroded through the formation of a solid iron fluoride  $\text{FeF}_2$  compound that selectively corroded the iron by forming tunnels in the base alloy. The nickel corroded next, leaving a copper-rich composition. The iron and nickel fluorides were converted to oxides outside of the metal phase. This then formed an adherent, electronically conducting nickel ferrite ( $\text{NiFe}_2\text{O}_4$ ) with copper inclusions being the last to corrode. The series of layers are clearly shown in the chemical phase patched map. In this test cell, the measured current efficiencies were above 90 pct for this type of cell design.

These observed reactions are consistent with a derived electromotive series for these metals in aluminum fluoride melts containing alumina. The penetration depth of the altered surface of the alloys initially varied following a power law with time to  $1/2$  power. The corrosion rate constant of the Cu:Ni:Fe alloy is about  $10^4$  smaller in NaF, KF, and  $\text{AlF}_3$  eutectic electrolytes at 973 K (700 °C) than at the 1223 K (950 °C) operating temperature of the Hall-Heroult process.

#### ACKNOWLEDGMENT

We thank Golden Northwest Aluminum Holding Company for permission to publish this work.

#### REFERENCES

1. J.C. Withers and G.V. Upperman: Patent US 4 342 637, 1982.
2. J.C. Withers and G.V. Upperman: Patent US 4 338 177, 1982.
3. T.R. Beck, J.C. Withers, and R.O. Loutfy: in *Light Metals 1984*, J. P. McGeer, ed., TMS, 1984, pp. 261-66.
4. J.D. Weyand, S.P. Ray, F.W. Baker, D.H. DeYoung, and G.P. Tarcy: "DOE (US Department of Energy)," Final Report, Alcoa Laboratories, Pittsburgh, PA, 1986.
5. T.R. Beck and R.J. Brooks: Patent US 4 865 701, 1989.
6. T.R. Beck: "NSF (US National Science Foundation)," Final Report, Electrochemical Technology Corp., Seattle, WA, 1993.
7. T.R. Beck: in *Light Metals 1994*, U. Mannweiler, ed., TMS, 1994, pp. 417-23.

8. T.R. Beck: in *Light Metals 1995*, J.W. Evans, ed., TMS, 1995, pp. 355–60.
9. D.R. Bradford: “DOE, Northwest Aluminum Technologies,” Final Technical Report, The Dalles, OR, 2005.
10. C.W. Brown: in *Light Metals 2000*, R.D. Peterson, ed., TMS, 2000, pp 391–96.
11. C.W. Brown: in *Light Metals 2003*, P. Crepeau, ed., TMS, 2003, pp. 293–98.
12. A.E. Bence and A.L. Albee: *J. Geol.*, 1968, vol. 76, pp. 382–403.
13. I.R. Harrowfield, C. MacRae, and N.C. Wilson: *Proc. 27th Annual Microbeam, Analysis Society (MAS) Meeting*, 1993, pp. 547–48.
14. N. Wilson, C. MacRae, and A. Torpy: *Microscop. Microanal.*, 2008, vol. 14, pp. 764–65.
15. HSC Chemistry for Windows, Version 3.0, 1997.
16. JANAF Thermochemical Tables, 2nd ed., U.S. National Bureau of Standards, Washington, DC, 1971.
17. J. Crank: *The Mathematics of Diffusion*, 2nd ed., Clarendon Press, Oxford, U.K., 1975.
18. E.A. Brandes, ed.: *Smithells Metals Reference Book*, 6th ed., Butterworths, London, U.K., 1983.
19. J. Frazer and J. Thonstad: unpublished research.
20. N. Ibl and J. Venczel: *Metalloberflache*, 1970, vol. 24, pp. 365–74.